water

MDPI

Article

Induced Polarization as a Proxy for CO_2-Rich Groundwater Detection—Evidences from the Ardennes, South-East of Belgium

Agathe Defourny [1,2,*], Frédéric Nguyen [1], Arnaud Collignon [2], Patrick Jobé [2], Alain Dassargues [1] and Thomas Kremer [3]

1 Urban and Environmental Engineering, Applied Sciences Faculty, University of Liège, Allée de la Découverte 9, 4000 Liège, Belgium; f.nguyen@uliege.be (F.N.); alain.dassargues@uliege.be (A.D)
2 Water Resource Department, Bru-Chevron S.A, La Bruyère 151, 4987 Stoumont, Belgium; a.collignon@spadel.com (A.C.); p.jobe@spadel.com (P.J.)
3 Laboratory of Planetology and Geodynamics, CNRS UMR-6112, Sciences and Techniques Faculty, University of Nantes, Rue de la Houssinière 2, 44322 Nantes, France ; thomas.kremer@univ-nantes.fr
* Correspondence: adefourny@uliege.be

Received: 2 April 2020; Accepted: 5 May 2020; Published: 14 May 2020

Abstract: CO_2-rich mineral groundwaters are of great economic and touristic interest but their origin and circulation paths in the underground are often poorly understood. A deeper understanding of the system plumbery and the development of non—to minimally—invasive near-surface geophysical methods for the prospection of potential productive areas is therefore of great interest to manage future supply. The objective of this contribution is to assess the ability of the time-domain induced polarization (TDIP) method, combined with the electrical resistivity tomography (ERT) method, to make the distinction between CO_2-rich groundwater from non-gaseous groundwater. Three combined ERT/TDIP tomographies were performed above known uplift zones in the south-east of Belgium where thousands of CO_2-rich groundwater springs exist. On all profiles, important contrasts in both electrical resistivity and chargeability distributions were observed in the vicinity of the upflow zone, also reflected in the normalized chargeability sections computed from the measured data. Low resistivity vertical anomalies extending in depth were interpreted as a saturated fracture network enabling the upflow of deep groundwater to the surface. High chargeability anomalies appearing directly close to the CO_2-rich groundwater springs were inferred to metallic oxides and hydroxides precipitation in the upper part of the aquifer, linked to pressure decrease and changing redox conditions in the up-flowing groundwater approaching the land surface. The combined interpretation of electrical resistivity and induced polarization datasets provides a very promising method for a robust prospection of CO_2-rich groundwater.

Keywords: CO_2-rich groundwater; hydrogeophysics; induced polarisation; mineral water; prospection

1. Introduction

Naturally sparkling mineral waters or CO_2-rich mineral waters occur in many places around the world, in various geological context most often associated to volcanic or mantellic activity. In Europe, CO_2-rich groundwater are observed in many regions of France [1,2], Germany [3], Poland [4], Italy [5], Portugal [6], for instance, but also overseas in Morocco [7], Australia [8] and South Korea [9], among others. Although they often trigger an intense economic and touristic activity (bottling, balneotherapy, spa and wellness), the detailed 'plumbery' of the system, the gas origin and its interactions with groundwater often remain unclear and constitute an active research topic.

CO_2-rich groundwater hydrogeological systems usually involve the same three elements: groundwater, a source of CO_2 and a fracture network favouring the upflow of CO_2-enriched groundwater to the surface. Natural CO_2 found in such groundwater (often referred to as geogenic CO_2) can have three potential origins: groundwater transfer through carbonated rocks (sedimentary origin), degradation of organic matter (biogenic origin) or degassing from the mantle (volcanic or juvenile origin) [10]. The identification of the CO_2 source is generally assessed through isotopic measurements ($\delta^{13}C$, $^3He/^4He$) and the natural CO_2 is most often assumed as coming from a deep origin where it was solubilized more easily in groundwater due to high pressures. Any network of deep fractures may then create a preferential pathway for CO_2-enriched groundwater to upflow towards the surface. To help understanding those systems and to ensure a sustainable management and protection of this resource, it is necessary to understand thoroughly the local geological and hydrogeological structure and behaviour of the main faulted zones.

In this context, non-intrusive geophysical methods are suitable exploration and imaging tools to assess the spatial distribution of different subsurface physical properties from which lithological, hydrogeological and structural information can be inferred. In particular, the electrical resistivity tomography (ERT) technique is an established method which produces a 2D or 3D estimation of the electrical resistivity spatial distribution within the subsurface. Within a same lithology, ERT is particularly sensitive to the presence of groundwater [11]. The ERT method has been shown to be very suited to the delineation of faults in fractured aquifers [12–16]. Data interpretation and image processing in such contexts are well mastered [17]. The information provided by ERT surveys is quite valuable to delineate saturated-faults systems. However, the method is not able to discriminate CO_2-rich groundwater from non-carbogaseous groundwater as the electrical resistivity contrast resulting from their different hydrochemical compositions may not be strong enough compared to other contrasts resulting from other subsurface variables (e.g., lithological variations).

In this paper, we investigate the use of another geo-electrical method called the time-domain induced polarization (TDIP) technique as a complementary method to ERT to detect, characterise and discriminate CO_2-rich groundwater springs from other springs [18]. The TDIP method is often used jointly with the ERT method since both data sets can be recorded simultaneously using the same acquisition system and field setup. Where the ERT aims at estimating the electrical conductive properties of the subsurface, the TDIP method focuses on studying the electrical capacitive properties of the subsurface (i.e., its ability to store electrical charges). In practice, a single TDIP measurement consists in applying a pseudo-DC electrical current through the ground during a period ranging from 1 to several seconds. During this injection time, ionic or electronic electrical charges are mobilised within the subsurface. Their movements will eventually lead to accumulation processes along the interfaces between the different phases composing the subsurface, a process usually referred to as polarization. Three types of polarization mechanisms are involved in TDIP surveys: the electrode polarization occurs in presence of metallic material, and usually exhibits the highest magnitude [19,20]. The membrane polarization is a structural phenomenon occurring when the pore space is particularly small, which is the case for example in the presence of clay minerals [21,22]. The dominant IP phenomenon in absence of metallic minerals or membrane structure is referred to as the electrical double layer polarization, which can be observed in any material as long as the ionic charges present in the saturating fluids have enough mobility, but whose magnitude is usually lower than the two previously quoted [23].

The purpose of the TDIP method is to estimate the spatial distribution of polarization processes and their magnitude, which we refer to in the following as the chargeability of the subsurface. High chargeability values indicate the occurrence of high magnitude polarization processes. TDIP was initially designed to help in the detection of metallic ore in mining activities [24], and is still largely used for this purpose today [25–27]. In the past decades, the method has also increasingly been used in environmental soil monitoring applications [28–32] and groundwater related investigations [33,34].

To our knowledge, the TDIP method has never been applied to the detection of CO_2-rich groundwater. However, a relatively close analogy can be found with characterization of geothermal

areas. For instance, [35] used the TDIP and ERT methods to track geochemical processes occurring in volcanic geothermal areas, and were able to distinguish between pyrite and iron-oxides minerals precipitating within the first 100 meters of the subsurface. The CO_2-rich groundwater context in which this study takes place is somehow similar as groundwater presents a high content in dissolved metallic species, in particular iron and manganese, the dissolution of the minerals from the host rock being favoured by the slight acidity of groundwater due to its high content in dissolved CO_2 [36]. If such minerals precipitate as groundwater upflows towards the land surface and oxidizes, those metallic precipitates could result in a significant TDIP contrast in upflow zones. Table 1 regroups a few chargeability values of ore minerals and rocks with various compositions. In this Table, studied samples have 1% concentration in the mineral of interest. Charging and discharging measuring times are about one minute each. Note that these conditions are specific to these laboratory experiments and the associated values should not be compared with field values.

Table 1. Table of indicative chargeability values for various types of ore minerals and rocks measured in laboratory experiments. Modified after [37–39].

Material Type	Chargeability (mV/V)	Material Type	Chargeability (mV/V)
Pyrrhotite	~10	20% Sulphides	2000–3000
Pentlandite	~10	8%–20% Sulphides	1000–2000
Pyrite	13.4	2%–8% Sulphides	500–1000
Copper	12.3	Volcanic tuffs	300–800
Graphite	11.2	Sandstone, Siltstone	100–500
Chalcopyrite	9.4	Dense volcanic rocks	100–500
Magnetite	2.2	Shale	50–100
Galena	3.7	Granite, Granodiorite	10–50
Hematite	0.0	Limestone, Dolomite	10–20

Our objective is to investigate the ERT and TDIP signals produced by CO_2-rich groundwater in the Ardennes region, where numerous springs of CO_2-rich groundwater exist and to assess the interest of combining these two methods for a better exploration and characterization of those specific hydrogeological systems. Three 2D ERT-IP profiles have been performed, in two different geological settings in the area (Cambro-Ordovician siliclastic rocks folded twice and Devonian sandstones folded once), either above a CO_2-rich spring emerging at the land surface or above abstraction wells effectively extracting CO_2-rich groundwater from the subsurface.

2. Geological Context

This study takes place in the Ardennes region, in the south-east of Belgium, where many natural sparkling water springs and thermal waters are known. The main city of the area, Spa, gave its name to the wellness and bathing traditions referred worldwide as “spa”.

The region is dominated by Palaeozoic rocks of the Rhenohercynian deformation zone that extends through Germany and Belgium, forming a fold-and-thrust belt, related to the Variscan orogeny (460 to 430 Myr) [40]. In the south eastern part of Belgium is found the Ardennes allochton, consisting of a Cambro-Silurian basement, mainly composed of dark clay and siltstone (evolving to slates in some zones), alternating with quartzites and quartzophyllads beds with thicknesses ranging from a few millimetres to several meters. The basement was reworked during the Caledonian orogeny (450 Myr) and is unconformably overlain by Devono-Carboniferous sandstones and limestones [41]. Basement rocks and the Devono-Carboniferous cover were then deformed during the Variscan orogeny (350 Myr) [42,43]. This deformation resulted in the NE-SW Ardenne anticlinorium, with outcropping Caledonian bedrock inliers located on anticline crests (Figure 1).

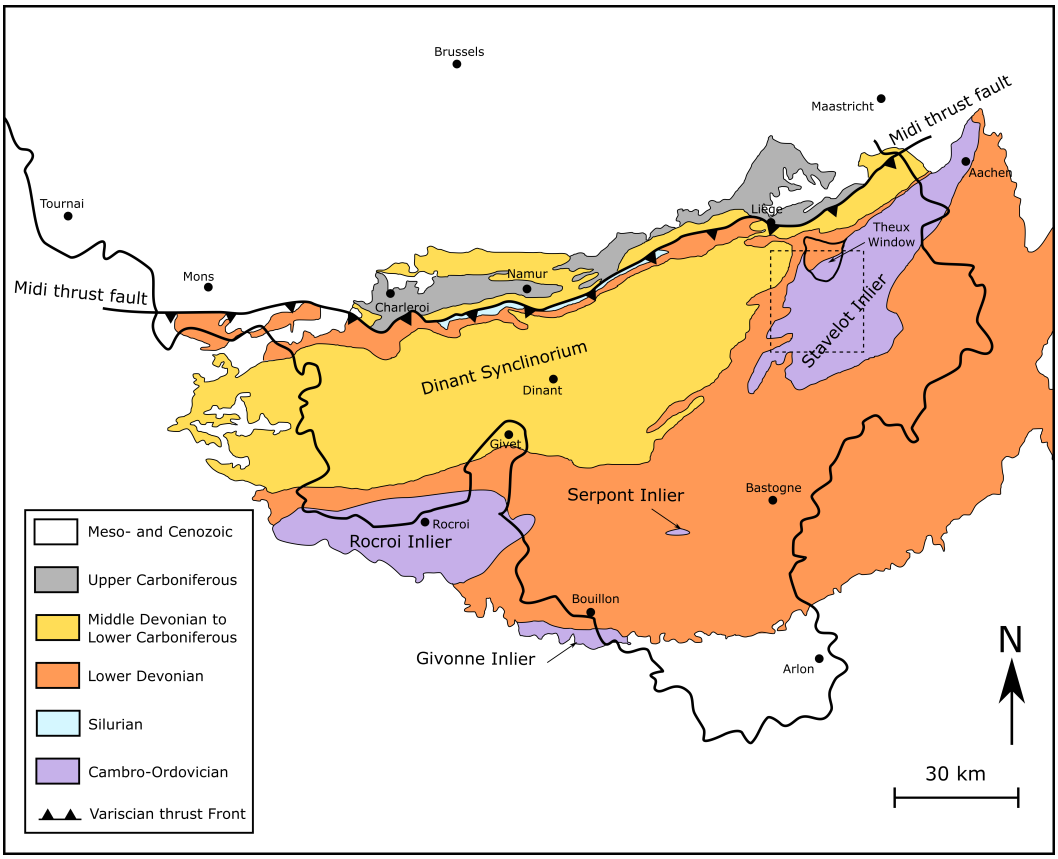

Figure 1. Regional geological context. The Stavelot Inlier is one of the inlier of the Ardenne anticlinorium formed by Cambro-Ordovician rocks unconformably overlaid by Devono-Carboniferous sandstones and limestones. The dashed rectangle indicates the study area (Figure 2) (modified after [44]).

The present study was conducted in the north western part of the largest of these inliers, the Stavelot Inlier. In this zone, the Malmedy Graben, a post-Variscian deformation caused by the collapse of the Rhine Graben is observed. The Malmedy Graben has a NE-SW orientation and is filled by Permian conglomerates [45] (Figure 2).

Aquifers in the area correspond to locally faulted and fractured quartzite beds resulting from the Caledonian and Variscan orogeneses. The slates being weathered in clayey deposits with lower permeabilities, they can be considered as low permeability barriers isolating aquifer compartments one from the others. The current knowledge does not allow to assess the origin of the CO_2 between a sedimentary or juvenile origin [46]. It is however assumed that the dissolution of CO_2 in groundwater is a continuous process occurring at several hundreds of meters in depth. Springs are located where the dense fracture network enables this CO_2-enriched groundwater to reach the surface. Groundwater samples show that water is rich in iron, which oxidizes to Fe^{3+} with atmospheric oxygen and then precipitates. Theses iron oxides and hydroxides give the spring a distinct orange-red colour, shown in Figure 3. These naturally ferruginous CO_2-rich springs, locally named 'pouhons', exist all over of the Stavelot Inlier (Figure 2) [42]. Hydrogen sulphide regularly accompanies CO_2 resulting in the typical smell. Pouhons are showing only a small part of the system, as we can easily assume that the major part of the iron-rich precipitates and the carbogaseous groundwater resources could be located in the shallow underground corresponding to the fractured bedrock under a semi-permeable colluvium.

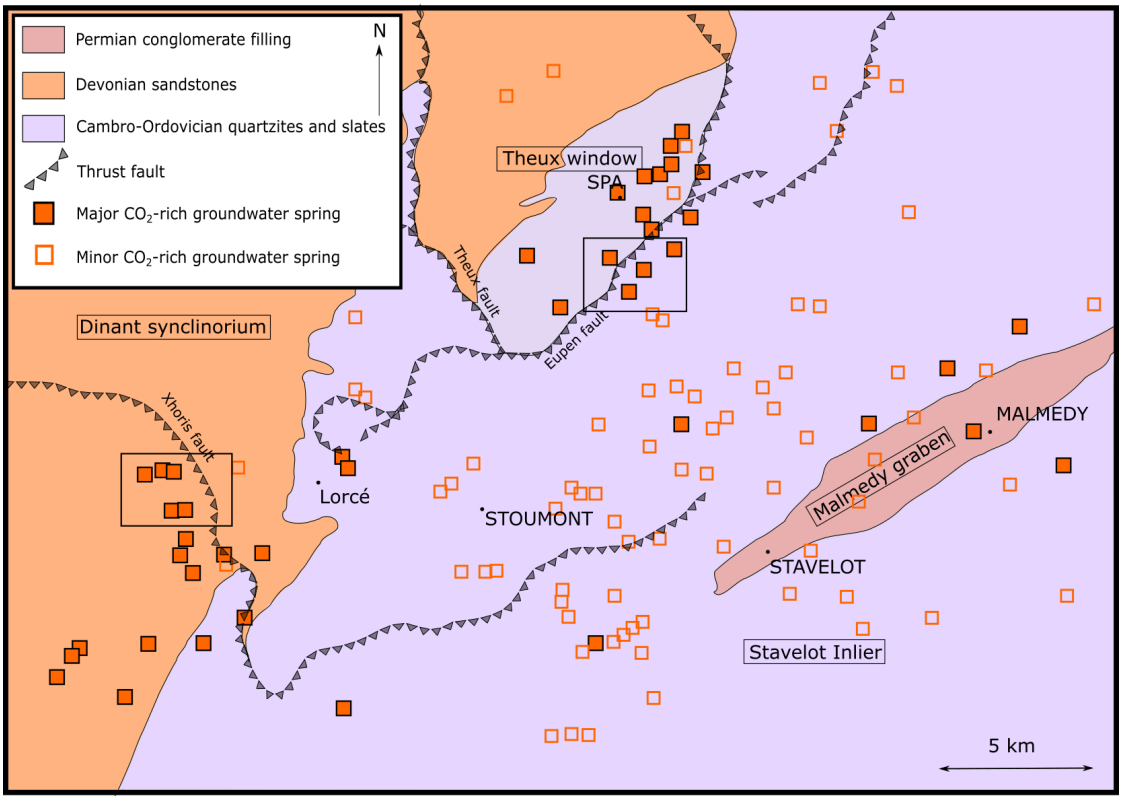

Figure 2. Location of the main CO_2-rich and ferruginous springs in the studied part of the Stavelot Inlier. Major springs are regularly visited and analysed, whereas minor springs are simply recognised. The position of both study sites is indicated by the black rectangles (see Figures 4 and 5).

Figure 3. CO_2-rich groundwater upflows to the surface, forming springs of naturally sparkling water. The springs present an intense orange-red colour due to the iron precipitation at the surface.

3. Experimental Sites

Three ERT/TDIP profiles were set up in two different study sites in the northern part of the Stavelot Inlier. Both areas present a particularly high density of naturally carbogaseous springs and several abstraction wells are in activity for CO_2-rich mineral water bottling.

The first site is located in the area of Stoumont (Lorcé), at the eastern border of the Stavelot Inlier, with an outcropping bedrock made of sandstones and shales from early Devonian. In the area is found

the major thrust fault of Xhoris (Figure 4). Many CO_2-rich groundwater natural springs are observed in the area, 94% of them located at a distance less than 250 m from a river.

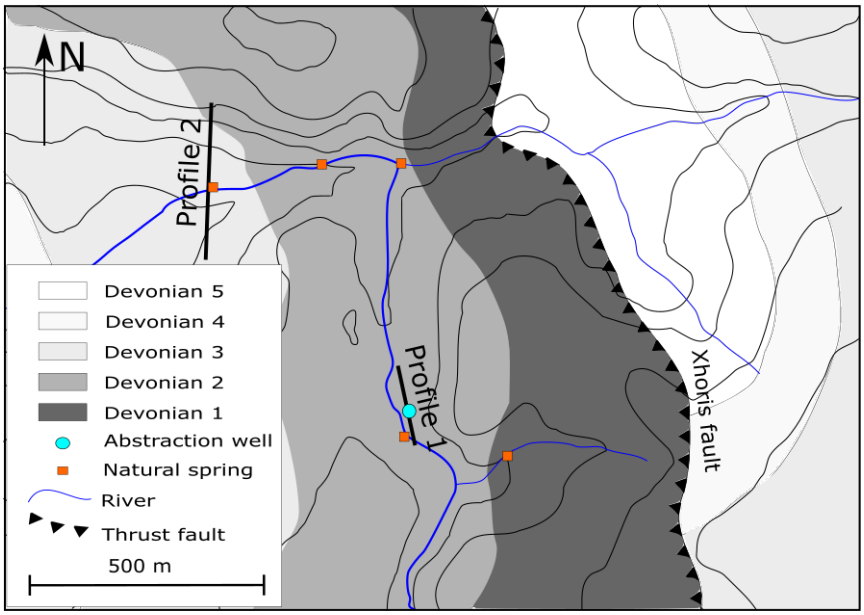

Figure 4. Localisation of Profile 1 and Profile 2 in the first studied site.

Two profiles have been performed in this area. The first one (Profile 1) was realised using 64 electrodes with a spacing of 5 m, for a total length of 315 m. The profile is located close to a naturally sparkling spring and an abstraction well producing 9 m^3/h of carbogaseous water. The second profile (Profile 2) was performed using 96 electrodes with a spacing of 5 m, for a total length of 475 m. It is centred straight above a sparkling groundwater spring.

The second site is located near the city of Spa, at the northern border of the Stavelot Inlier, where the outcropping bedrock is composed of an alternation of dark shales and quartzites from the Cambrian to Ordovician, folded twice. Numerous thrust faults are known in the area. Superficial Cretaceous deposits are found on the plateau forming the southern limit of the site (Figure 5).

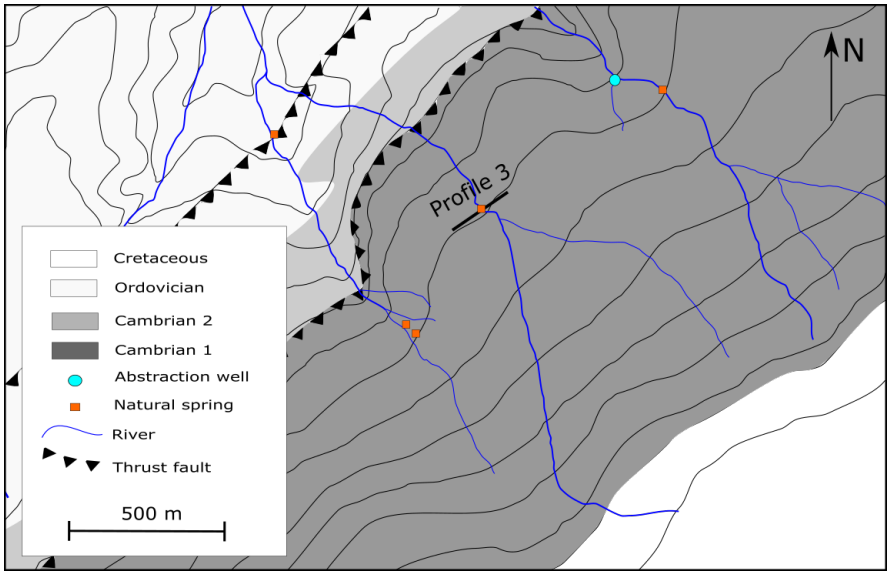

Figure 5. Localisation of Profile 3 in the second studied site.

A third (Profile 3) was performed in this area, using 64 electrodes with a spacing of 5 m, for a total length of 315 m. This profile was performed right upon a naturally sparkling spring and crossing a river.

4. Materials and Methods

ERT and TDIP are both based on the same acquisition set-up, and as such, can be performed simultaneously. The difference between the two methods lies on their focus on different parts of the recorded electrical voltage (Figure 6) and thus on different electrical properties of the subsurface. The ERT method provides information about the electrical conductive properties of the underground (i.e., its ability to let electrical current flow). The data of interest are usually the apparent resistivity of the subsurface or the resistance, which are linked with Equation (1), where I is the injected current intensity, V_0 is the total measured voltage and K is a geometric factor related to the electrodes positions. This set of apparent resistivity can be inverted to obtain an estimation of the true electrical resistivity distribution within the subsurface.

$$\rho_a = K\frac{V_0}{I} \tag{1}$$

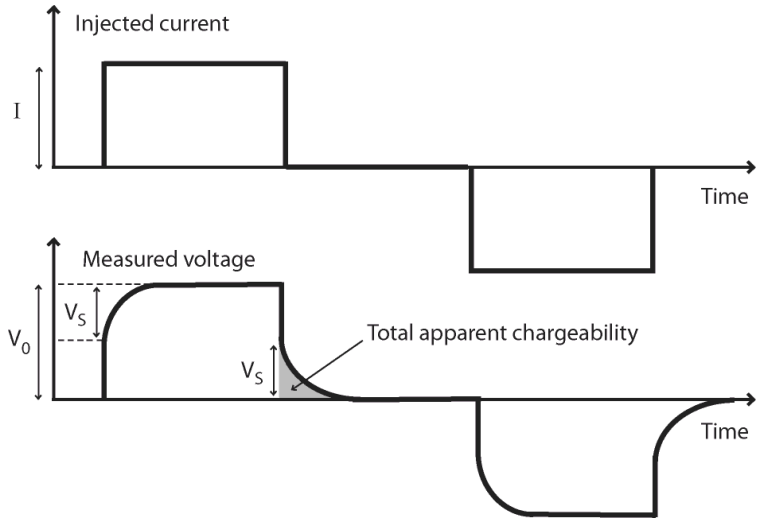

Figure 6. Illustration of an electrical measurement. A pseudo-DC electrical current under the form of square signals with alternate polarities (for error estimation) is injected, producing a voltage signal. The maximum voltage amplitude V_0 is used to compute the apparent resistivity and the decaying secondary voltage V_S is used to compute the apparent chargeability (modified after [47]).

The TDIP method provides information about the electrical capacitive properties of the underground (i.e., its ability to temporarily store electrical charges). When an electrical current is injected into the subsurface, several polarization processes can occur due to the movement of electrical charges. These mechanisms imply a redistribution of charges along interfaces, creating a secondary electrical field which itself results in a secondary voltage V_S (Figure 6) that can be measured. When the injected current is cut-off, V_S follows a decay curve as the charges progressively return to electrical equilibrium. The characteristics of this decay curve are used to compute an apparent chargeability value, which reflects the magnitude of the polarization processes. To do so, the decaying signal V_S is generally integrated over n time windows, and the apparent chargeability M is calculated following Equation (2), in which $V_s(t)$ is the secondary voltage decaying with time, V_0 is the voltage

used for calculating the DC resistivity and t_i and t_{i+1} are the open and close times of the time window over which the signal is integrated [48,49].

$$M = \sum_{i=1}^{n} \frac{1}{V_0(t_{i+1} - t_i)} \int_{t_i}^{t_{i+1}} V_s(t)dt \quad (2)$$

Then again, applying an inversion process [50], the apparent chargeability distribution is transformed into an estimation of the true chargeability values of the ground. For additional details about the ERT and the TDIP methods, the involved physical processes behind the signals, how to implement them in the field and to process the data, we refer the reader to [49,51–53].

4.1. Acquisition Parameters

In this study, the resistivity and chargeability measurements were all performed from the surface as 2D linear tomographic acquisition, which we will refer to as 2D profiles. For each profile, the apparent resistivity and the apparent chargeability distributions have been measured together using the Terrameter LS (ABEM) device. The characteristics of each profile are presented in Table 2 along with the number of iterations used for the inversion process and the root-mean-square (RMS) error values associated with the final resistivity and chargeability models.

Table 2. Acquisition and inversion parameters for the three 2D profiles.

	Profile 1	**Profile 2**	**Profile 3**
Length (m)	315	615	315
♯ electrodes	64	126	64
Electrode spacing (m)	5	5	5
Presence of spring or abstraction well	Spring + Well (9 m^3/h)	Spring	Spring
♯ iterations	4	4	4
RMS resistivity (%)	2.87	2.88	2.84
RMS chargeability (%)	4.38	2.54	2.64

For each measurement, the current injection duration was 1.7 s, the IP integration period was 3.6 s divided in 17 log-distributed windows and the delay between two current injections was set to 0.5 s in order to let enough time for the medium to return to electrical equilibrium. All profiles were performed using stainless steel electrodes, because the large dimensions of the profiles, the high number of electrodes and the nature of the ground surface (sometimes hard to dig through) prevented us to use non-polarizable electrodes which are often more delicate to handle. The measuring protocol was a multiple-gradient array, which is well suited for fast multi-channels data acquisition as it provides a balanced sensitivity to vertical and horizontal structures and a good signal-to-noise ratio [54,55].

4.2. Data Processing and Inversion

A disadvantage of using metallic electrodes for current injection and voltage measurements can be the increased risk of occurrence of parasitic effects linked to electrode polarization phenomena that may affect the shape of the secondary voltage decay [56]. To account for this risk and filter our data sets accordingly, the apparent chargeability data associated with noisy decaying curves were disregarded. Each curve was visually inspected and rejected if the global curvature did show an expected smoothly decreasing shape. Figure 7a represents the limit case in which the data was accepted while Figure 7b) proposes a histogram based representation of the data statistic distributions. Moreover, negative chargeability curves were removed from the data set because most of them presented a significantly noisy shape and keeping this data systematically resulted in a significant increase of the inverted models RMS error (sometimes above 10%). As a result of those data selection criteria, a maximum of 13% of the data set was removed for all profiles.

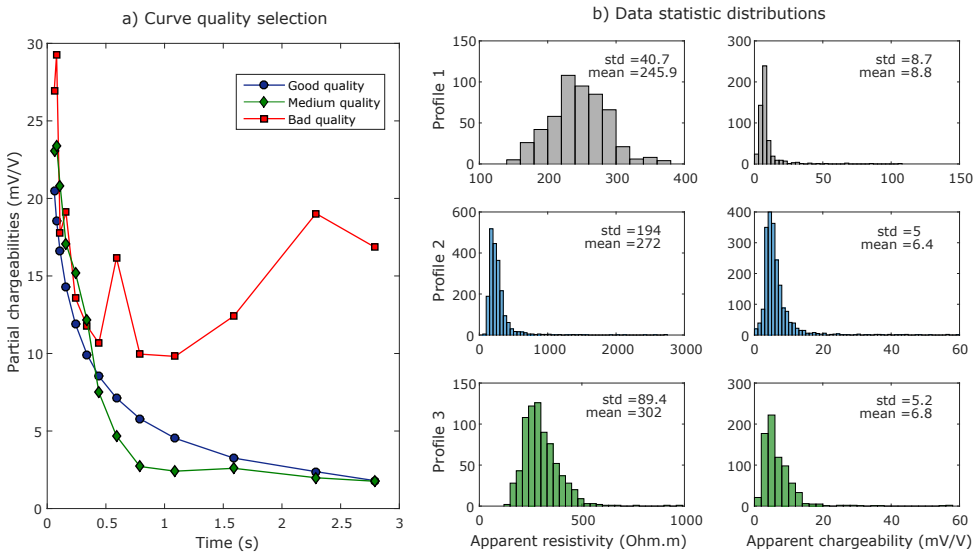

Figure 7. (**a**) Example of three chargeability curves indicating different data quality. The medium quality type of curve is accepted during the filtering but considered as the extreme case. (**b**) Statistical distributions of apparent chargeability and resistivity data for the three profiles. Mean and standard deviation values are indicated for each histogram.

After this processing, the apparent resistivity and the apparent chargeability data were inverted using the commercial software Res2Dinv [57,58], using a least-square smooth inversion with a Gauss-Newton scheme and a laterally extended and refined grid model. We used a separate inversion scheme where the TDIP data is inverted using only the final model of the ERT inversion. At each iteration the relative change in RMS error is computed and the inversion stops when this percentage is below 5%. The final RMS values obtained for all profiles were low (<5%) and denoted a satisfying match between models and data. After inversion, the estimated resistivity and chargeability distributions were used to compute the normalized chargeability distribution of the underground, following Equation (3):

$$M_n = \frac{m}{\rho} \tag{3}$$

where M_n is the normalized chargeability calculated on one block of the inverted model and m and ρ are respectively the chargeability and resistivity value on the same block of the inverted models. The normalized chargeability is a very useful parameter in TDIP surveys since it represents mainly the strength of the ground polarization [49], whereas the chargeability values of the ground are related to both the conductive and capacitive properties of the studied medium.

5. Results

Resistivity, chargeability and normalized chargeability sections are presented for each profile. On each section, a black dashed line represents the limit below which the depth of investigation (DOI) index, as defined by Oldenburg et al. (1999), exceeds a value of 0.2, which is considered as the threshold value above which the associated inversion results are uncertain [59]. The sensitivity values, which can also inform us on the confidence that can be attributed to the results are displayed in Appendix A (Figure A1). On each normalized chargeability section, the main anomalies are labelled with a number corresponding to the profile, and a letter for later reference in the paper.

5.1. Profile 1

Profile 1 is located above CO_2 rich abstraction well.

Figure 8 shows the inverted resistivity, chargeability and normalized chargeability distributions, respectively, obtained with the ERT/TDIP data set recorded on Profile 1, centred on a 36 m deep abstraction well which produces CO_2-rich water. No geological log was recorded during the drilling operations but the geological knowledge of the area suggests that the subsurface at this location is mainly composed of an alternation of fractured sandstones, quartzites and siltites. The well is equipped with a PVC casing. The static piezometric level in the well is 2.5 m deep. The vadose zone is expected to be thin in the vicinity of the profile and cannot be imaged due to the relatively low resolution associated with a 5 m electrode spacing. It can however be safely assumed that the three distributions observed on Figure 8 correspond to water-saturated geological formations.

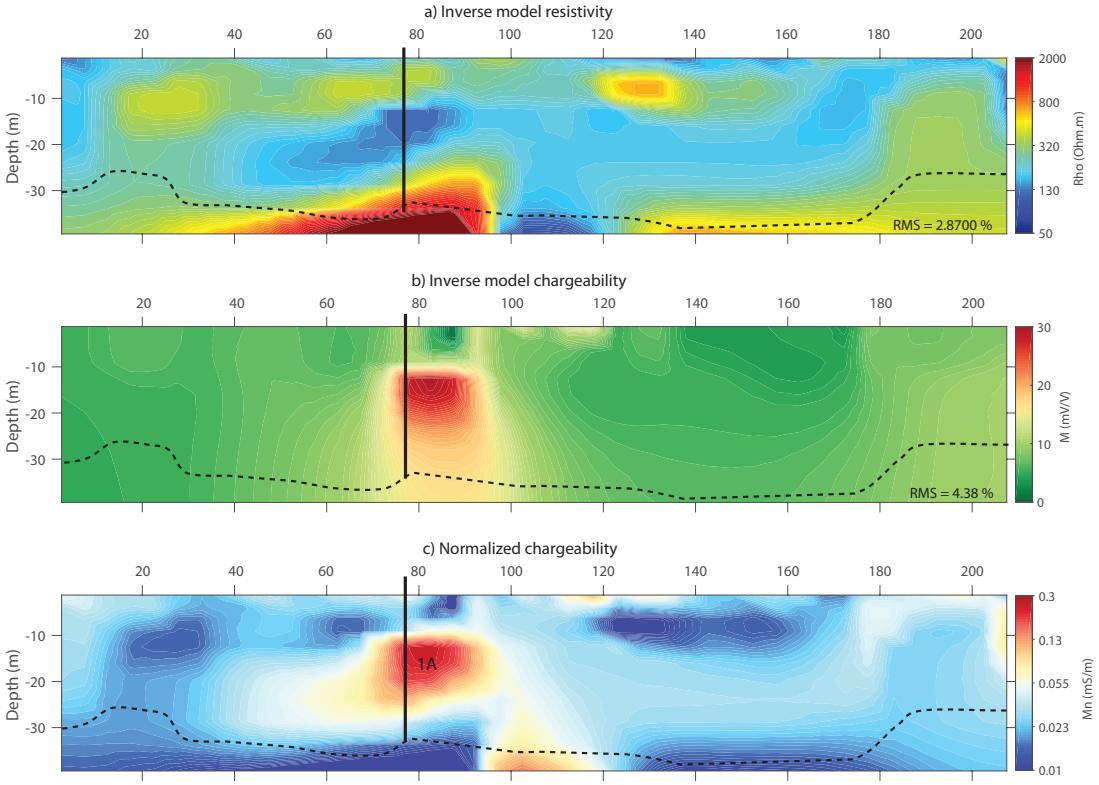

Figure 8. Resistivity, chargeability and normalized chargeability distributions in Profile 1. The straight black line corresponds to the 36 m depth abstraction well which produces CO_2-rich water. Horizontal positions are given in *m*. The dashed black line indicates the limit below which the depth of investigation (DOI) value exceeds the trust threshold value of 0.2. The main normalized chargeability anomaly is numbered 1A.

The resistivity distribution shows that the first 30 m of the subsurface are composed of formations with resistivity ranging from about 100 Ω.m to 500 Ω.m, such values being consistent with an alternation of sandstones, quartzites and siltites, most likely partially weathered and saturated with water (see [60] for reference resistivity values and [12,14,61] for examples of ERT surveys on weathered rock formations). Below 30 m depth, the sharp resistivity increase suggests that rocks with lower porosity and connectivity are reached, probably corresponding to non-weathered formations. Note that regarding the low sensitivity the high DOI values (>0.2) at those depths, this interpretation cannot be considered as certain.

The chargeability distribution on Figure 8 shows a high chargeability anomaly (about 30 mV/V) in the central part of the section, from 10 m to about 30 m depth. This anomaly is located in the vicinity of the abstraction well. Elsewhere, chargeability values are globally constant, around 7 mV/V.

The conjunction of the resistivity and chargeability distribution finally leads to the normalized chargeability distribution which eliminates the effect of resistivity upon chargeability values and provides a spatial representation of the sole polarization processes magnitude. In this case, the image suggests that strong polarization processes are occurring in a zone located between 155 and 180 m on the x-axis and between 10 and 30 m in depth. This anomaly is correlated with the chargeability anomaly observed on Figure 8b. A strong normalized chargeability anomaly is also observed in depth (about 35–40 m), suggesting the presence of polarizable material in this area, although again, the low sensitivity at those depths requires caution. We interpret the central anomaly as being linked to the presence or circulation of CO_2-rich groundwater.

5.2. Profile 2

Profile 2 is located above a CO_2-rich groundwater spring.

Figure 9 shows the inverted resistivity, chargeability and normalized chargeability distributions of Profile 2. The profile is centred on a natural CO_2-rich groundwater spring, emerging on the bank of a small river which crosses the profile perpendicularly at 35 m south of the spring. The topography of Profile 2 is quite significant, with elevation variations up to more than 50 m between the centre of the profile (x = 300 m) and the northern end of the profile (x = 615 m). The geological composition consists in an alternation of pink quartzites, sandstones and shales [62].

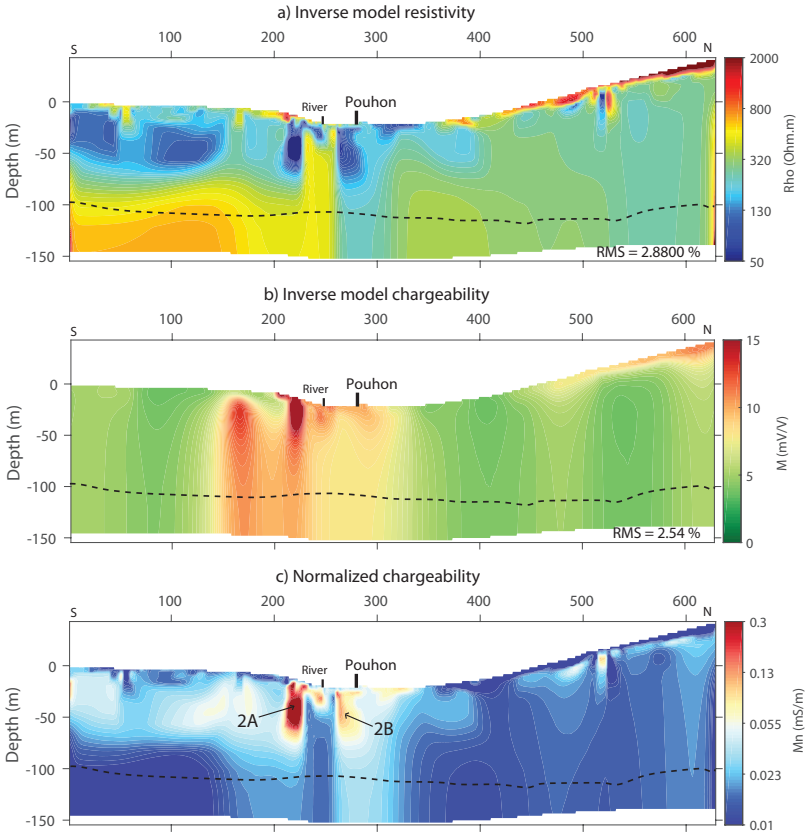

Figure 9. Resistivity, chargeability and normalized chargeability distributions in Profile 2. The location of the pouhon is indicated. Horizontal positions are given in *m*. The dashed black line indicates the limit below which the DOI value exceeds the trust threshold value of 0.2. The two main normalized chargeability anomalies are numbered 2A and 2B.

In the centre of the profile, at the lowest topographical point, permanent wetlands are observed suggesting that the piezometric level is reaching the surface in this area. In the northern part of the profile, many quartzite outcroppings can be observed, explaining the high resistivity features located at the surface on the right part of this profile (Figure 9). Below this surface formation which is less than 10 to 15 m thick, the resistivity decreases to much lower values (about 200 Ω.m), indicating rock formations probably weathered and saturated. In the southern part of the profile, fewer resistive features are observed at the surface and low resistivity values ($\leqslant$100 Ω.m) are reached reached quickly, suggesting a piezometric level close to the surface in this area. Below these conductive zones, rock formations with higher resistivity values seem to be reached at about 100 m depth, both on the southern and northern parts of the profile, whereas in the central part of the profile the low resistivity zone extends deeper. As in Profile 1, this deep low resistivity corridor suggests the existence of a weathered zone extending in depth allowing the upflow of water and possibly CO_2-rich water up to the surface. In addition, the DOI for Profile 2 indicates that inversion results are trustworthy down to 100 m depth.

In terms of chargeability, we observe as expected relatively high chargeability values correlated with the highly resistive quartzites on the northern side of the valley. Those anomalies are not, however, linked with the presence of polarizable materials, but are solely due to the presence of high resistivity rocks. Indeed, they tend to disappear on the normalized chargeability section. The most interesting features observed on the chargeability section are located in the vicinity of the spring: two high chargeability anomalies (close to 50 mV/V), about 20 m thick and 15 m wide are located close to the spring at about 10 to 15 m depth. Given the excellent DOI and sensitivity values, those observations are reliable and confirm that a significant amount of polarizable material is located in this area, supporting the idea of a preferential hydraulic pathway for the upflow of CO_2-rich water from a deep, low resistivity, weathered area leading to precipitation of metallic minerals close to the surface. We rule out the possibility that the presence of the river itself is related to these anomalies, because two other TDIP/ERT profiles performed a few hundred meters from Profile 2 and also crossing the river did not exhibit any similar anomaly (Appendix C).

5.3. Profile 3

Profile 3 is located above a CO_2-rich groundwater spring.

Figure 10 shows the inverted resistivity, chargeability and normalized chargeability distributions obtained for Profile 3. This profile is also centred above a 'pouhon' where ferruginous, CO_2-rich water emerges at the surface at the location $x = 155$ m. The geological context here is somehow different than for Profiles 1 and 2. The main geological structures are expected to be composed of an alternation of quartzite banks, sometimes pyritic, generally between 20 cm to 50 cm thick and of slate beds.

A thin layer with medium resistivity values is observed at the surface possibly corresponding to the unsaturated zone. Below, resistivity values are lower (about 100 to 200 Ω.m), suggesting a saturated weathered rock aquifer of about 35–40 m thickness in the central part of the profile. Below these weathered formations, high resistivity areas are reached, which most likely correspond to unaltered rock with low permeabilities. However, this unweathered rock is again not continuous as a lower resistivity area is observed at roughly between 75 m and 150 m along the x axis. This area could correspond to a zone with higher permeability values, where deep origin CO_2-rich groundwater might be up-flowing towards the surface eventually resulting in the occurrence of the pouhon.

The chargeability distribution seems to globally follow the main changes in the resistivity distribution. However, computing the normalized chargeability reveals that several horizontally shaped, high values anomalies of about 10 to 15 m thickness are detected all along the profile between 20 m and 40 m in depth. In this case, the normalized chargeability values are somehow lower than in Profiles 1 and 2, but still indicate the occurrence of significant polarization processes, which could also support the scenario of a preferential upflow of CO_2-rich groundwater leading to precipitation close to the surface. However, this interpretation may also be discussed given the geological context of Profile 3, where the presence of slates could also be the cause of these anomalies.

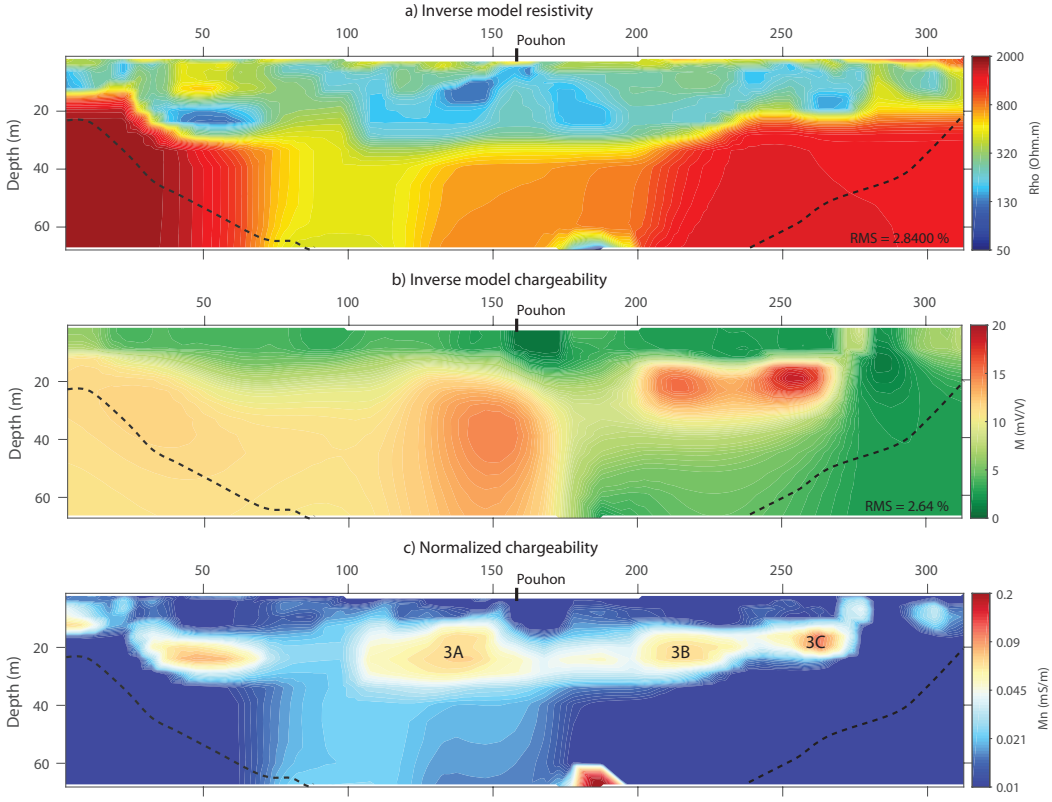

Figure 10. Resistivity, chargeability and normalized chargeability distributions in Profile 3. The location of the pouhon is indicated. Horizontal positions are given in *m*. The dashed black line indicates the limit below which the DOI value exceeds the trust threshold value of 0.2. The 3 main normalized chargeability anomalies are numbered 3A, 3B and 3C.

6. Discussion

Our results show that similarities exist between the three different profiles, both in terms of resistivity distribution and chargeability distribution. Regarding the resistivity distributions, the most striking feature observed in all three cases is the systematic conductive anomaly embedded within the resistive deep formation. We interpret this as an area where the rock formation is fractured, allowing the preferential upflow of deep water. In all three cases, chargeability and normalized chargeability anomalies of high magnitude are observed in areas close to the pouhon or the abstraction well. Our interpretation is that those anomalies originate from the presence of precipitated metallic (mostly iron) minerals as a consequence of CO_2-rich groundwater upflow and oxidation. In the following part, the hydrogeological and hydrogeochemical aspects of this phenomenon are discussed, and a framework to correctly identify whether a normalized chargeability anomaly can be attributed to the presence of iron minerals is proposed.

6.1. Iron Oxides and Hydroxides as Markers of CO_2-Rich Groundwater Circulation

CO_2-rich groundwaters are ruled by carbonates equilibrium that regulates their concentrations in several elements. The introduction of CO_2 in groundwater results in groundwater acidification as carbonic acid is formed. Groundwater capacity to lixiviate the host rock is then enhanced and metallic minerals as pyrite (FeS_2) or pyrrhotite ($Fe_{1-x}S$, $0 < x < 0.2$), Fe-rich minerals that are common in the studied area are dissolved more easily. Table 3 provides the results of hydrochemical analysis performed on water samples collected from the springs and wells located near the profiles. Similar groundwater compositions are reported by Modelska et al. (2015) and Operacz et al. (2018) [63,64], who both studied known CO_2-rich springs located in the Carpathians region in Poland.

Comparable hydrochemical observations are also reported by Jeong et al. (2005) [65] on some CO_2-rich springs located in South Korea. Chae et al. (2016) [66] reports similar compositions (low pH (<6) and moderate electrical conductivity (<1000 μS/cm) in 18 springs around the world. Those similarities indicate that the geophysical tools and interpretation processes presented here are likely applicable to other regions in the world where CO_2-rich springs are present.

Table 3. Hydrochemistry data for the springs and the well upon which the profiles are located.

Parameter	Profile 1	Profile 2	Profile 3
Type of spring	Well	Pouhon	Pouhon
pH [-]	5.9	5.8	5.6
EC [μS/cm]	223	863	138
Eh [mV]	107	81	
Ca^{2+} [mg/L]	23.9	46.6	12.8
Mg^{2+} [mg/L]	10.76	30.3	4.5
Na^{+} [mg/L]	5.6	104	6.7
K^{+} [mg/L]	1.07	5.09	0.82
SiO_2 [mg/L]	7.1	9.8	8.6
HCO_3^{-} [mg/L]	100	414	59
Fe total [mg/L]	7.5	8.4	4.4
Mn total [mg/L]	0.48	0.76	0.14
Dissolved CO_2 [g/L]	0.77	2.32	0.37
Dissolved O_2 [g/L]	2.5	5.8	

Under the pH conditions (between 4 and 6 pH units) and Eh conditions (between −0.3 and +0.2 V) prevailing in these areas, iron is almost exclusively found under the form Fe^{2+}. As groundwater upflows and enters a more oxidizing zone, Fe^{2+} rapidly oxidizes to Fe^{3+}, as detailed in Equation (4). It precipitates under the hydroxide form ($Fe(OH)_3$, mostly goethite), as shown in Figure 11. The degassing of CO_2 at the atmospheric pressure further leads to the formation of $Fe(OH)_3$ as the pH increases.

$$4Fe^{2+} + O_2 + 10H_2O \rightleftharpoons 4Fe(OH)_3 + 8H^+ \quad (4)$$

In the presence of dissolved carbonates and bicarbonates in groundwater, the following reaction also exists (Equation (5)).

$$4Fe(HCO_3)_2 + O_2 + 10H_2O \rightleftharpoons 4Fe(OH)_3 + 8CO_2 \quad (5)$$

Following Equation (4), 0.14 mg of O_2 are needed to oxidize 1 mg of Fe^{2+} and thus produce 1.92 mg of $Fe(OH)_3$. In the area, average dissolved oxygen content of groundwater was measured on the field with a multi-parameter probe and ranges between 1 and 3 mg/L whereas dissolved Fe concentrations, measured through ICP-MS analysis, in CO_2-rich waters are ranging between 10 and 20 mg/L. It appears that the oxygen content in groundwater, although low, is sufficient to yield to Fe hydroxides precipitation. Goethite is most occurring precipitated iron mineral at the surface at the spring locations.

This interpretation is also supported by the observation that all chargeability and therefore normalized chargeability anomalies that we associate to the presence of CO_2-rich groundwater are located at relatively shallow depths (typically between 10 m and 30 m depth for Profiles 1, 2 and 3), where oxygen content is expected to be high enough to enable the iron oxidation. Deeper, under more reducing conditions, Fe^{2+} stay dissolved in groundwater.

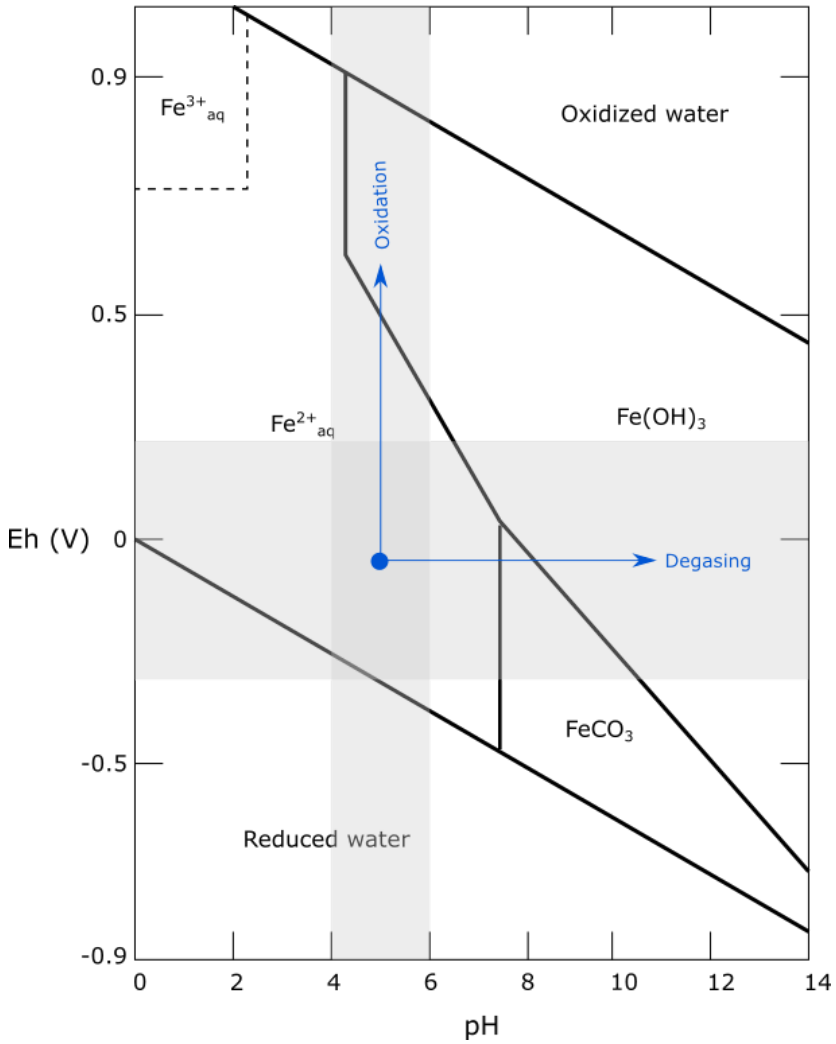

Figure 11. Eh-pH diagram ruling redox equilibria associated with iron species in the presence of CO_2. Solid lines represent aqueous/solid boundaries whereas dashed lines represent aqueous/aqueous boundaries. The grey areas represent the pH and Eh conditions prevailing in groundwater in the study areas. The figure shows that when reaching the surface, the combined groundwater oxidation and CO_2 degassing lead to the formation and precipitation of $Fe(OH)_3$ (mostly under the form of goethite) (Modified form [67]).

6.2. Geoelectric Signature of CO_2-Rich Groundwater Circulation

Analysing the results from Profiles 1, 2 and 3, and following the hydrochemical conditions described above, the best indicator of CO_2-rich groundwater circulation is the presence of a normalized chargeability anomaly, which reflects both groundwater circulation and presence of polarizable iron hydroxides that are known to produce an observable TDIP effect [68,69]. The normalized chargeability parameter has the advantage to compare the magnitude of polarization processes between areas where the underground resistivity is significantly different. Indeed, if the subsoil is highly resistive, high chargeability will be measured which will not be the result of polarization processes. The results from Profiles 2 and 3 are a good example of how the normalized chargeability representation only highlights the areas where the chargeability anomalies are effectively due to polarization processes.

Hence, in the context of CO_2-rich groundwater exploration, a high normalized chargeability value will ideally be associated to a low resistivity anomaly (indicating water circulation in connected/weathered porous media) combined with a relatively high chargeability anomaly (associated in this case to the presence of metallic precipitates). However, such a case may also

occur in different geological contexts, for example in a saturated clay layer, which will be highly conductive and will also yield relatively high chargeabilities.

This aspect is illustrated in Figure 12, where a large number of typical normalized chargeability values encountered in different publications involving field TDIP measurements have been collected. These values are organised in 4 different groups depending on the cause invoked by the authors to explain the observed anomalies. The group "Metallic minerals" refers to anomalies associated with the presence of disseminated metallic minerals, the group "Landfill" relates to TDIP studies dedicated to imaging landfill extension and where the reported anomalies are attributed to the presence of waste. The group "Clay rocks" involves the presence of clay material as a cause for chargeability anomalies. The publications associated with those three groups are all summarised in Table 4. In addition, the "CO_2-rich groundwater" group gathers all the values associated with the normalized chargeability anomalies observed on Profile 1, 2 and 3 in this study, respectively numbered from 1A to 3C. Finally, a single value forms the group "Non-carbogaseous groundwater", which corresponds to an anomaly recorded on another profile in the study area, where groundwater was not over-saturated in CO_2 (more details about this profile in Appendix B).

Table 4. Summary of the IP surveys used in Figure 12. Many of those studies did not indicate the signal injection and integration time. For those who did, injection periods range from 1 to 4.4 s and integration times range from 0.6 to 3.6 s.

Reference	Context of Survey	Interpretation
[70]	Pb-Zn deposit	Sulphides (galena, sphalerite, pyrite and marcasite)
[26]	manganese deposits	manganese deposits (pyrite, chalcopyrite),Fe oxides
[71]	Gold exploration	Disseminated sulphides (pyrite, chalcopyrite),iron oxides
[34]	Water exploration	Sand with heavy minerals
[72]	Detecting cracks in clay rocks	13% Pyrite in calcite rock
[73]	Detection of ore bodies	
[74]	Metalliferrous veins exploration	Presence of Barite and Galena
[75]	Plutonic rock mineral exploration	Sulphure mineralizations
[76]	Plutonic rock mineral exploration	Ore deposits
[77]	Galena exploration	Pyrite, chalcopyrite, galena
[35]	Volcanic geothermal area	Pyrite, iron oxides
[78]	Case study alluvial fans	High clay content
[47]	Hydrocarbon contamination	Clayey silt
[34]	Water exploration	Weathered rock leaching clay minerals
[79]	Slope study	Clay
[72]	Detecting cracks in clay rocks	Clay rocks
[80]	Landfill characterization	Clayey till
[52]	Mapping of lithotypes	Clay till
[81]	Landfill characterization	Waste, plastic and metal
[82]	Landfill characterization	Waste, soil with leachate
[80]	Landfill characterization	Waste and leachate
[83]	Landfill characterization	Waste

Figure 12a illustrates the difficulty of interpreting normalized chargeability data when no in-situ information is available. Except for the group Landfill that is well distinguished from the others and could possibly be discriminated based only on the normalized chargeability values, all the other groups are mixed together with values approximately in the range [0.01–1] mS/m.

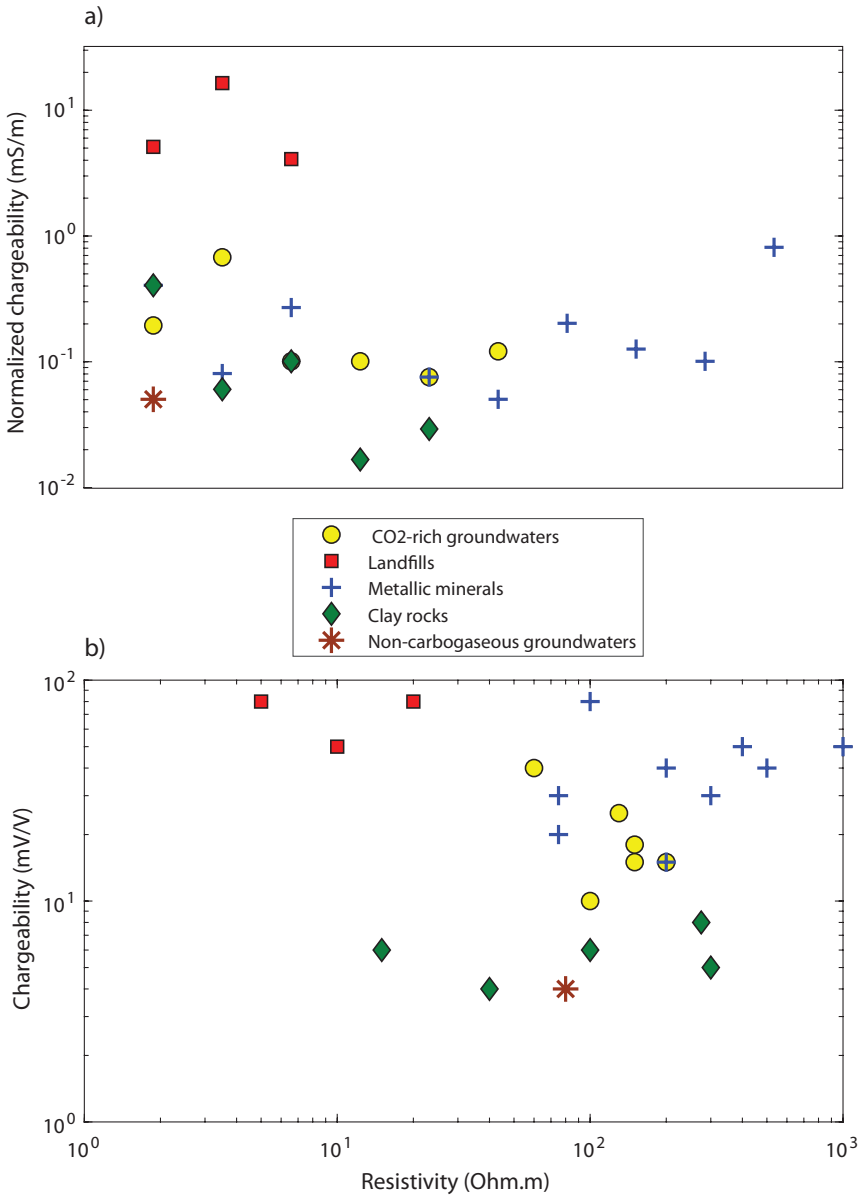

Figure 12. (**a**) Logarithmic representation of the normalized chargeability values produced by different geological contexts. (**b**) Representation of these anomalies in the chargeability vs. resistivity space.

However, Figure 12b shows that representing the normalized chargeability values within the chargeability-resistivity space allows a better discrimination. The group Metallic minerals is well separated from the group Clay rocks, and the group Landfill is also isolated. From this point of view, the anomalies measured in a CO_2-rich groundwater context are located in the same graphic area as the group Metallic minerals, supporting the assumption that the dominant cause for IP effect in the CO_2-rich groundwater environment is indeed the presence of disseminated metallic precipitates. Moreover, the anomaly associated with Non-carbogaseous groundwater is located at the same level as the Clay rocks group, far from CO_2-rich groundwater anomalies. This also suggests that representing normalized chargeability anomalies in the chargeability-resistivity space may help discriminate CO_2-rich groundwater from non-carbogaseous waters. Using the data gathered here, a standard range of values can be proposed for the discrimination of CO_2-rich groundwater springs with the ERT/TDIP method. The data presented here suggests that in the studied geological context, the presence of CO_2-rich groundwater within the subsurface is realistic when chargeability values are at least above 10 mV/V. Below this threshold value, the origin of a normalized chargeability anomaly

is either due to the presence of clay, or simply to a very conductive zone characterized by weathered formations where non-gaseous groundwater is circulating.

Although geophysical studies have already been performed to investigate CO_2-rich spring systems (e.g., [84,85]), they always focused on delineating water circulation paths and aquifer structural properties without considering the potentially carbogaseous nature of groundwater. To our knowledge, the normalized chargeability signature of CO_2-rich springs provided by the TDIP method is the first geophysical framework allowing to discriminate CO_2-rich from non-carbogaseous groundwaters.

7. Conclusions and Further Research

Based on the presented results and discussion, the combination of induced polarization and electrical resistivity tomography measurements was shown as providing a new proxy for detection of CO_2-rich groundwaters. Indeed, in the local geological context, the resistivity and chargeability distributions yield specific markers of the presence of groundwater and of precipitated iron minerals, respectively. Both signatures are needed to attest the occurrence of exploitable CO_2-rich groundwater resources, but the latest is the true marker for CO_2-rich groundwaters. We assume that the presence of chargeability anomalies is linked to the presence of iron hydroxides, iron being leached from the hosting rocks by groundwater acidified by the presence of dissolved CO_2. Iron hydroxides then precipitate when CO_2-rich groundwater reaches the oxidising zone in the upper part of the subsurface. Since goethite is the first precipitated iron hydroxide and subsequently is the most observed mineral at the spring locations, we supposed that the presence of this metallic hydroxide leads to the observed chargeability anomalies and we provide a detailed hydrogeochemical framework backing up this interpretation and explaining our results. For exploration purposes, the normalized chargeability anomalies are the most striking parameter for detection of CO_2-rich groundwaters and anomalies values should be examined within the chargeability-resistivity space.

Although geophysical anomalies linked to the presence of CO_2-rich groundwater appears to be quite clear in the studied area, it also raises new questions to be addressed in order to fully understand the involved processes. First, a different sub-surface configuration could yield to different geoelectrical signatures. However, while high chargeability anomalies due to mineral precipitation are likely to be a common marker in many or all situations, resistivity features could be more case-dependent. In future work, the geoelectrical signature of CO_2-rich groundwater occurrences in different geological contexts will be investigated in order to provide a broader understanding of their electrical response. Secondly, although goethite has been observed in several spring locations, its presence in shallow depths must be confirmed by drilling sampling operations. Lab tests will be performed to measure its intrinsic chargeability. Finally, a broader understanding of groundwater circulation and upflow in the area is necessary. The introduction of chemistry in our multivariate analysis and the further development of a full hydrogeochemical model could explain pathways of groundwater, changes in compositions and redox conditions. Finally, as we assumed that the upflow of CO_2-rich groundwater is linked to the presence of faults and fractures, the use of combined ERT-TDIP profiles in 3D and at larger scales would be of great interest to further delineate these fractures.

Author Contributions: Conceptualization: T.K. and F.N.; methodology: T.K., A.D. (Agathe Defourny) and F.N.; software, A.D. (Agathe Defourny) and T.K.; validation, all authors; formal analysis, A.D. (Agathe Defourny) and T.K.; investigation, A.D. (Agathe Defourny) and T.K.; resources, F.N.; data curation, T.K.; writing—original draft preparation, A.D. (Agathe Defourny) and T.K.; writing—review and editing, A.D. (Alain Dassargues), F.N., A.C. and P.J.; visualization, A.D. (Agathe Defourny); supervision, F.N. and A.D. (Alain Dassargues); project administration, T.K.; funding acquisition, A.C. and P.J. All authors have read and agreed to the published version of the manuscript.

Funding: This research was co-funded by SPW Région Wallonne of Belgium and company Bru-Chevron S.A.(Spadel S.A.) under grant number 7984. The authors acknowledge these two institutions for their support.

Conflicts of Interest: The authors declare no conflict of interest. The funders had no role in the design of the study; in the collection, analyses, or interpretation of data; in the writing of the manuscript, or in the decision to publish the results.

Appendix A. Sensitivity Distributions of ERT/TDIP Profiles

Figure A1 shows the normalized sensitivity distributions associated with Profiles 1, 2 and 3. As it is usually observed in ERT/TDIP surveys, the sensitivity values are lower toward the extremities of the 2D section, and are decreasing with depth.

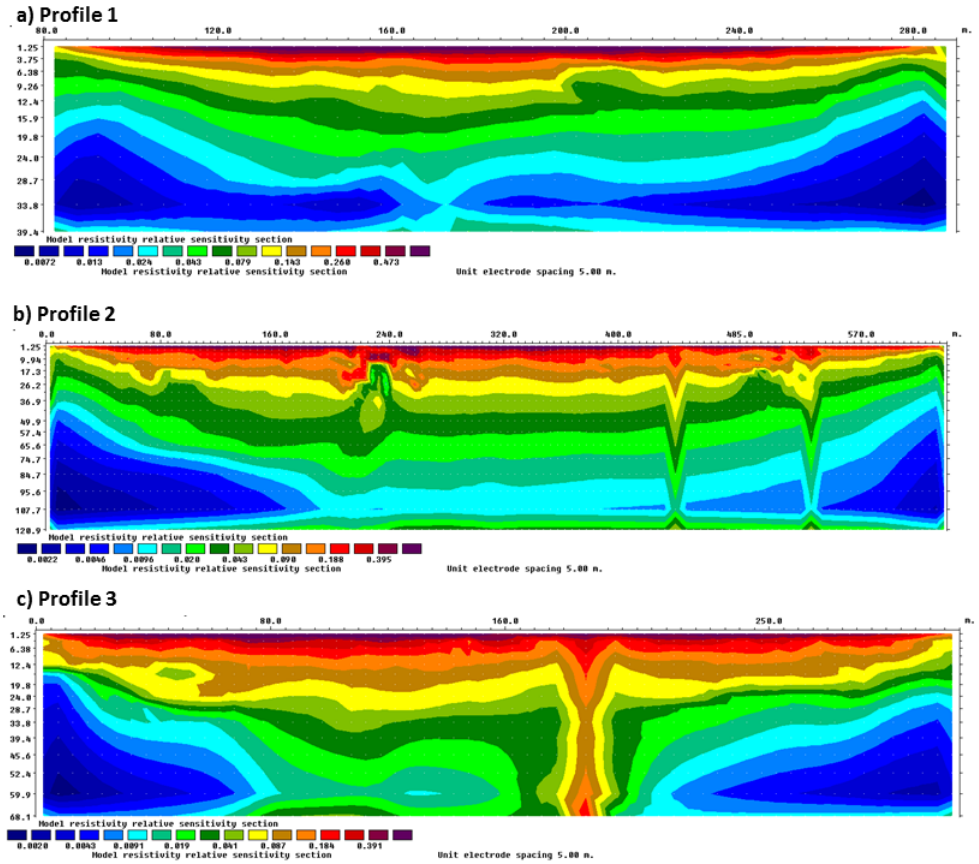

Figure A1. Normalized sensitivity distribution associated with the ERT/TDIP Profiles 1, 2 and 3.

Appendix B. ERT/TDIP Anomalies Associated with Non-carbogaseous Groundwater

Figure A2 shows the inverted resistivity, chargeability and normalized chargeability distribution, respectively, obtained with an ERT/TDIP data set recorded in the same area as Profile 2. We refer to this profile as Non-carbogaseous water profile. It was acquired during a large exploration campaign in the area, where 12 ERT/TDIP profiles (including Profile 2) were realised to explore for CO_2-rich groundwater springs. Profile 2 was performed centred on the known pouhon location, as a base reference for the characterization of CO_2-rich groundwater springs. Among the 11 other profiles, the Non-carbogaseous-water profile showed a promising evidence of a potential uplift zone due to the presence of a very clear resistivity vertical contrast, being interpreted as a fracture and leading to a relatively high normalized chargeability anomaly (from 50 to 100 m). The chargeability values were however quite low, around the background level. Based on this observation, an exploration well was drilled, which turned out to be productive, with an exploitation rate fixed at 6 m^3/h after several weeks of pumping. This rate is similar to what is observed in other wells in the area. However, no dissolved carbonic gas could be detected in the analysed samples. The water presents a pH of 6.3 which is higher than what it generally observed in CO_2-rich groundwater in the region. The electric conductivity value of 160 μS/cm is mostly influenced by the concentration in bicarbonates (90 mg/L). Fe and Mn concentration are respectively of 8.9 and 0.7 mg/L, which is consistent with what can be found in CO_2-rich groundwater springs of the area, although in the lower part of the concentrations range for Fe.

This experience showed that high values normalized chargeability anomaly alone may not suffice to discriminate CO_2-rich groundwater, and that the combined presence of a low resistivity anomaly and in particular of a high chargeability anomaly is needed.

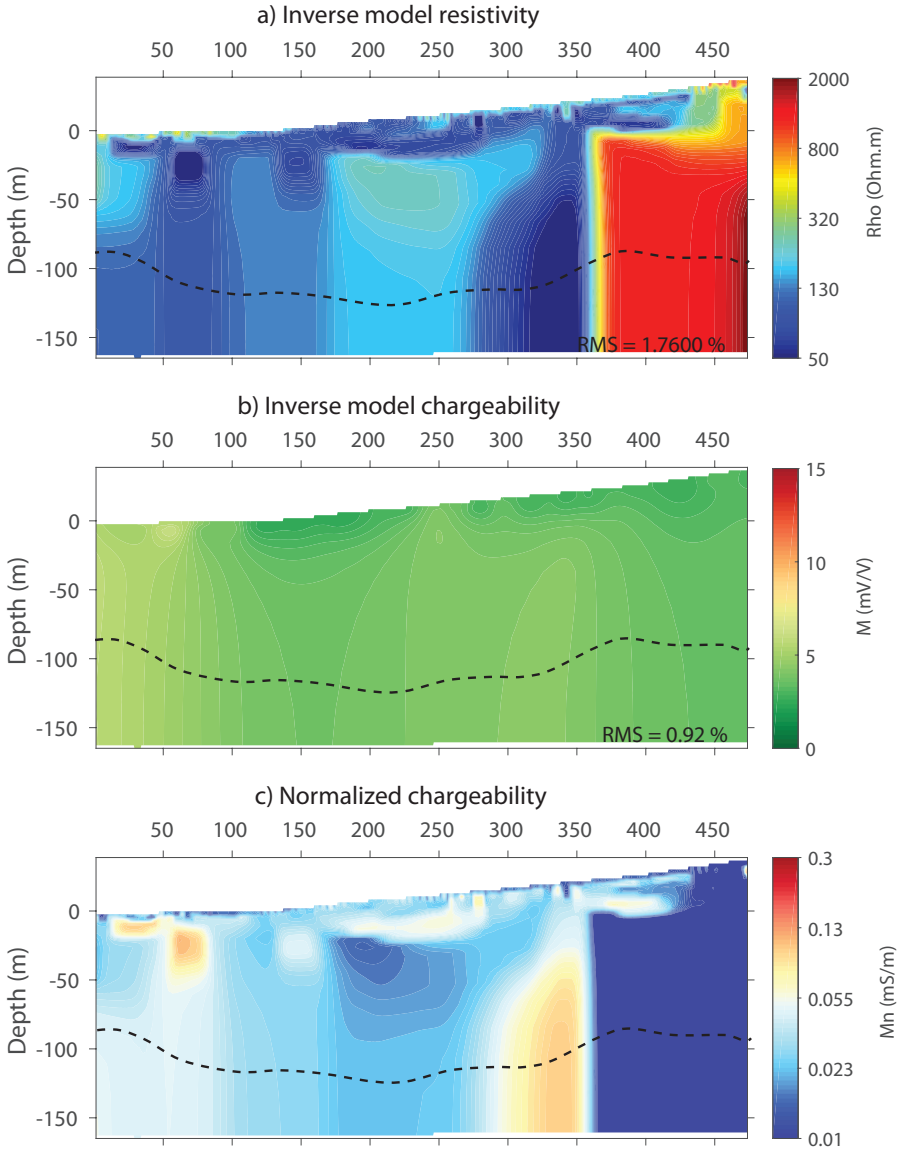

Figure A2. Resistivity, chargeability and normalized chargeability distributions obtained in the same area as profile 2. The dashed black line indicates the limit below which the DOI index value exceeds the trust threshold value of 0.2.

Appendix C. Effect of the Presence of the River

Two ERT-TDIP profiles were also performed a few hundred meters from profile n1, which both crossed the river. Figure A3 shows a comparison between the normalized chargeability distribution of the three profiles. A high value anomaly is observed for Profile 1, whereas no particular anomaly is observed for the two other profiles at the location of the river crossing. This indicates that the anomaly observed on Profile 12 is not an artifact related to the presence of the river.

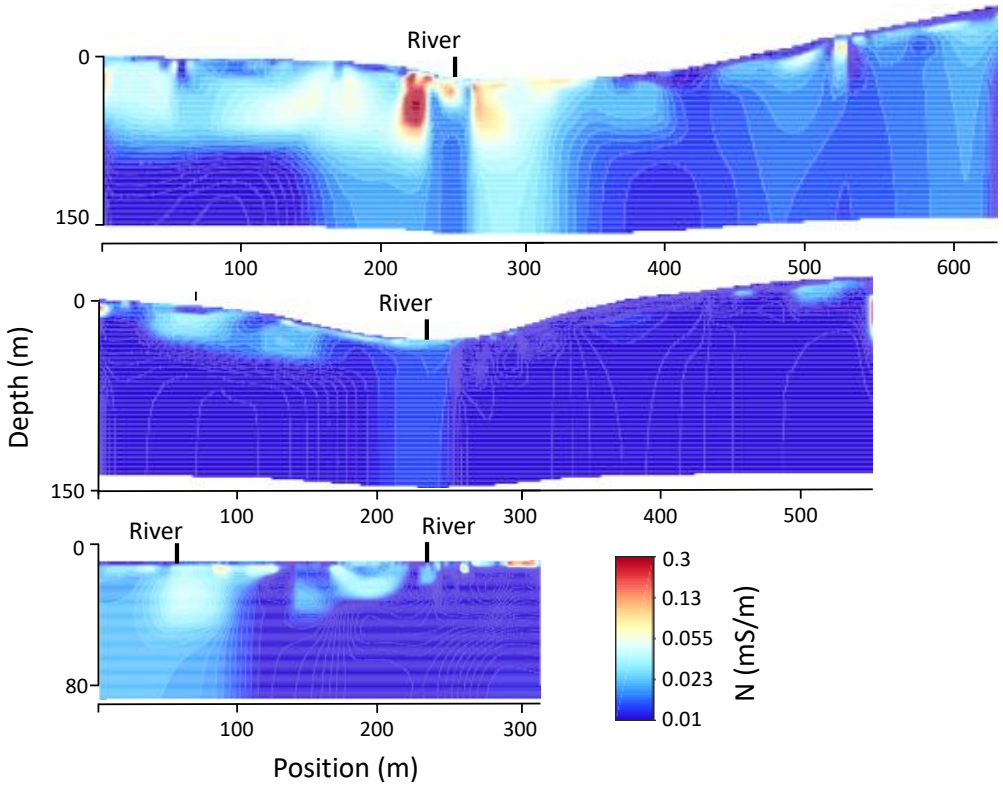

Figure A3. Normalized chargeability distributions. Up: Profile 1, Middle: additional profile perpendicular to the river and Down: additional profile globally parallel to the river, which crosses the river in two locations.

References

1. Dewandel, B.; Alazard, M.; Lachassagne, P.; Bailly-Compte, V.; Coueffe, R.; Grataloup, S.; Ladouche, B. Respective roles of the weathering profile and the tectonic fractures in the structures and functioning of crustalline thermo-mineral carbo-gaseous aquifers. *J. Hydrol.* **2017**, *547*, 690–707.
2. Marechal, J.; Lachassagne, P.; Ladouche, B.; Dewandel, B.; Lanini, S.; Strat, P.L.; Petelet-Giraud, E. Structure and hydrogeochemical functioning of a sparkling natural mineral water system determined using a multidisciplinary approach: A case study from southern France. *Hydrogeol. J.* **2014**, *22*, 47–68.
3. Goepel, A.; Lonschiniski, M.; Viereck, L.; Buchel, G.; Kukowski, N. Volcano-tectonic structures and CO2-degassing patterns in the Laccher See basin, Germany. *Int. J. Earth Sci.* **2015**, *104*, 1483–1495.
4. Lesniak, P.M. Origin of carbon dioxide and evolution of CO_2-rich waters in the West Carapathians, Poland. *Acta Geol. Pol.* **1998**, *48*, 343–366.
5. Grassa, F.; Capasso, G.; Favara, R.; Inguaggiato, S. Chemical and isotopic composition of waters and dissolved gases in some thermal springs of Sicily and adjacent volcanic islands, Italy. *Pure Appl. Geophys.* **2006**, *163*, 781–807.
6. Carreira, P.; Marques, J.; Carvalho, M.; Nunes, D.; da Silva, M.A. Carbon isotopes and geochemical processes in CO_2-rich cold mineral water, N-Portugal. *Environ. Earth Sci.* **2014**, *71*, 2941–2953.
7. Tassi, F.; Vaselli, O.; Moratti, G.; Piccardi, L.; Minissle, A.; Poreda, R.; Huertas, A.D.; Bendkik, A.; Chenakeb, M.; Tedesco, D. Fluid geochemistry versus tectonic setting: The case study of Morocco. *Geol. Soc. Lond. Spec. Publ.* **2006**, *262*, 131–145.
8. Shugg, A. Hepburn Spa: Cold carbonated mineral waters of Central Victoria, South Eastern Australia. *Environ. Geol.* **2008**, *58*, 1663–1673.
9. Choi, H.; Woo, N.C. Natural analogue monitoring to estimate the hydrochemical change of groundwater by the carboating process from the introduction of CO2. *J. Hydrol.* **2018**, *562*, 318–334.
10. Honnegger, J.; Gadalia, A. Exploitation des eaux minérales carbo-gazeuses. *Houille Blanche* **1995**, *2*, 106–110.

11. Rubin, Y.; Hubbard, S. *Hydrogeophysics*; Springer Science & Business Media: Cham, Switzerland, 2006; Volume 50.
12. Gao, Q.; Shang, Y.; Hasan, M.; Jin, W.; Yang, P. Evaluation of a weathered rock aquifer using ERT method in South Guangdong, China. *Water* **2018**, *10*, 293.
13. Robinson, J.; Slater, L.; Johnson, T.; Shapiro, A.; Tiedeman, C.; Ntarlagiannis, D.; Lane, J. Imaging pathways in fractured rock using three-dimensional electrical resistivity tomography. *Groundwater* **2016**, *5*, 186–201.
14. Robert, T.; Dassargues, A.; Brouyère, S.; Kaufmann, O.; Hallet, V.; Nguyen, F. Assessing the contribution of electrical resistivity tomography (ERT) and self-potential (SP) methods for a water well drilling program in fractured/karstified limestones. *J. Appl. Geophys.* **2011**, *75*, 42–53.
15. Ball, L.B.; Ge, S.; Caine, J.S.; Revil, A.; Jardani, A. Constraining fault-zone hydrogeology through integrated hydrological and geoelectrical analysis. *Hydrogeol. J.* **2010**, *18*, 1057–1067.
16. Yadav, G.; Singh, S. Integrated resistivity surveys for delineation of fractures for groundwater exploration in hard rock areas. *J. Appl. Geophys.* **2007**, *62*, 301–312.
17. Nguyen, F.; Sand, D.; Jongmans, S.G.; Pirard, E.; Loke, M. Image processing of 2D resistivity data for imaging faults. *J. Appl. Geophys.* **2005**, *57*, 260–277.
18. Binley, A.; Kemna, A. DC resistivity and induced polarization methods. In *Hydrogeophysics*; Springer: Cham, Switzerland, 2005; pp. 129–156.
19. Revil, A.; Aal, G.A.; Atekwana, E.; Mao, D.; Florsh, N. Induced polarization response of porous media with metallic particles—2: Comparison with a broad database of experimental data. *Geophysics* **2015**, *80*, 539–552.
20. Mao, D.; Revil, A. Induced polarization response of porous media with metallic particles—Part 3: A new approach to time-domain induced polarization tomography. *Geophysics* **2016**, *81*, 345–357.
21. Waxman, H.V.M. Induced polarization of shaly sands. *Geophysics* **1984**, *49*, 1267–1287.
22. Weller, A.; Slater, L.; Nordsiek, S. On the relationship between induced polarization and surface conductivity: Implications for petrophysical interpretation of electrical measurements. *Geophysics* **2013**, *78*, 315–325.
23. Chelidze, T.; Gueguen, Y. Electrical spectroscopy of porous rocks: A review—I. Theoretical models. *Geophys. J. Int.* **1999**, *137*, 1–15.
24. Bleil, D. Induced polarization: A method of geophysical prospecting. *Geophysics* **1953**, *18*, 636–661.
25. Mansoor, N.; Slater, L. On the relationship between iron concentration and induced polarization in marsh soils. *Geophysics* **2006**, *72*, 1–5.
26. Moreira, C.; Borges, M.; Vieira, G.; Filho, W.; Montanheiro, M. Geological and geophysical data intergration for delimitation of mineralized areas in a supergene manganese deposits. *Geofis. Int.* **2012**, *53*, 403–416.
27. Srigutomo, W.; Trimadona.; Pratomo, P. 2D Resistivity and Induced Polarization Measurement for Manganese Ore Exploration. *J. Phys. Conf. Ser.* **2016**, *739*, 012138, doi:10.1088/1742-6596/739/1/012138.
28. Carlson, N.R.; Hare, J.L.; Zonge, K.L. Buried landfill delineation with induced polarization: Progress and problems. In Proceedings of the SAGEEP, 14th EEGS Symposium on the Application of Geophysics to Engineering and Environmental Problems, Denver, CO, USA, 4–7 March 2001; Volume 20.
29. Kemna, A.; Binley, A.; Slater, L. Crosshole IP imaging for engineering and environmental applications. *Geophysics* **2004**, *69*, 97–107.
30. Gazoty, A.; Fiandaca, G.; Pedersen, J.; Auken, E.; Christiansen, A. Mapping of landfills using time-domain spectral induced polarization data: The Eskelund case study. *Surf. Geophys.* **2012**, *10*, 575–586.
31. Dafflon, B.; Wu, Y.; Hubbard, S.; Birkholzer, J.; Daley, T.; Pugh, J.; Trautz, R. Monitoring CO_2 intrusion and associated geochemical transformations in a shallow groundwater system using complex electrical methods. *Environ. Sci. Technol.* **2012**, *47*, 314–321.
32. Kremer, T.; Schmutz, M.; Agrinier, P.; Maineult, A. Laboratory monitoring of CO_2 injection in saturated silica and carbonate sands using spectral induced polarization. *Geophys. J. Int.* **2016**, *207*, 1258–1272.
33. Aizebeokhai, A.; Oyeyemi, K.; Joel, E. Electrical resistivity and induced-polarization imaging for groundwater exploration. In Proceedings of the SEG Technical Program Expanded Abstracts, Dallas, TX, USA, 16–21 October 2016; Society of Exploration Geophysicists: Houston, TX, USA, 2016; pp. 2487–2491.
34. Chrindja, F.J.; Dahlin, T.; Steinbruch, F. Reconstructing the formation of a costal aquifer in Nampula province, Mozambique, from ERT and IP methods for water prospection. *Environ. Earth Sci.* **2017**, *76*, 36.

35. Levy, L.; Maurya, P.; Byrdina, S.; Vandemeulebrouck, J.; Sigmundsson, F.; Arnason, K.; Labazuy, P. Electrical Resistivity Tomography and Time-Domain Induced Polarization field investigations of geothermal areas at Krafla, Iceland: comparison to borehole and laboratory frequency-domain electrical observations. *Geophys. J. Int.* **2019**, *218*, 1469–1489.
36. Wollast, R.; Wollast, A. Etude géochimique des eaux carbogazeuses de la région de Stoumont. *Les Eaux Souterraines en WALLONIE, Bilan et Perspectives-ESO 87*; Région Wallonne of Belgium: Namur, Belgium, 1987.
37. Oldenburg, D.; Li, Y. Inversion for applied geophysics: A tutorial. *Investig. Geophys.* **2005**, *13*, 89–150.
38. Airo, M. Geophysical signatures of mineral deposit types. *Geol. Surv. Finl. Spec. Pap.* **2015**, *58*, 9–70.
39. King, A.; Milkereit, B. Review of geophysical technology for Ni-Cu-PGE deposits. In Proceedings of Fifth Decennial International Conference on Mineral Exploration, Toronto, ON, Canada, 9–12 September 2007; Decennial Mineral Exploration Conferences: Toronto, ON, Canada, 2007; Volume 7, pp. 647–665.
40. Vanbrabant, Y.; Braun, J.; Jongmans, D. Models of passive margin inversion: Implications for the Rhenohercynian fold-and-thrust belt, Belgium and Germany. *Earth Planet. Sci. Lett.* **2002**, *202*, 15–29.
41. Hance, L.; Dejonghe, L.; Ghysel, P.; Laloux, M.; Mansy, J. Influence of heterogeneous lithostructural layering on orogenic deformation in the Variscan Front Zone (eastern Belgium). *Tectonophysics* **1999**, *309*, 161–177.
42. Goemaere, E.; Demarque, S.; Dreeseen, R.; Declercq, P.Y. The Geological and Cultural Heritage of the Caledonien Stavelot-Venn Massif, Belgium. *Geoheritage* **2016**, *8*, 211–233.
43. Belanger, I.; Delaby, S.; Delcambre, B.; Ghysel, P.; Hennebert, M.; Laloux, M.; Marion, J.; Mottequin, B.; Pingot, J. Redéfinition des unités structurales du front varisque utilisées dans le cadre de la nouvelle Carte Géologique de Wallonie (Belgique). *Geol. Belg.* **2012**, *15*, 169–175.
44. Herbosch, A.; Liégeois, J.P.; Pin, C. Coticules of the Belgian type area (Stavelot-Venn Massif): Limy turbidites within the nascent Rheic oceanic basin. *Earth-Sci. Rev.* **2016**, *159*, 186–214.
45. Geukens, F. Strike skip deformation des deux cotés du Graben de Malmédy. *Ann. De La Société Géologique De Belg.* **1995**, *118*, 139–146.
46. Debbaut, V.; Cajot, O.; Ruthy, I.; Dassargues, A.; Hanson, A.; Bouezmarni, M. *Aquifères de l'Ardenne*; Academia Press: Gent, Belgium, 2014.
47. Blondel, A. Développement des méThodes géOphysiques Électriques pour la Caractérisation des Sites et Sols Pollués aux Hydrocarbures. Ph.D. Thesis, Ecole Doctorale Montaigne-Humanités, Pessac, France, 2014.
48. Schön, J. *Physical Properties of Rocks: Fundamentals and Principles of Petrophysics*; Elsevier: Amsterdam, The Netherlands, 1996; Volume 65.
49. Slater, L.; Lesmes, D. Electrical-hydraulic relationships observed for unconsolidated sediments. *Water Resour. Res.* **2002**, *38*, 31-1.
50. Aster, R.; Borchers, B.; Thurber, C. *Parameter Estimation and INVERSE Problems*; Elsevier: Amsterdam, The Netherlands, 2018.
51. Binley, A.; Slater, L.; Fukes, M.; Cassiani, G. Relationship between spectral induced polarization and hydraulic properties of saturated and unsaturated sandstone. *Water Resour. Res.* **2005**, *41*, 12.
52. Gazoty, A.; Fiandaca, G.; Pedersen, J.; Auken, E.; Christiansen, A. Data repeatability and acquisition techniques for time-domain spectral induced polarization. *Surf. Geophys.* **2013**, *11*, 391–406.
53. Loke, M.; Kuras, O.; Chambers, J.; Rucker, D.; Wilkinson, P. Instrumentation, Electrical Resistivity. In *Encyclopedia of Solid Earth Geophysics*; Gupta, H.K., Ed.; Springer International Publishing: Cham, Switzerland, 2020; pp. 1–7.
54. Dahlin, T.; Zhou, B. Multiple-gradient array measurements for multichannel 2D resistivity imaging. *Surf. Geophys.* **2006**, *4*, 113–123.
55. Aizebeokhai, A.; Oyeyemi, K. The use of the multiple-gradient array for geoelectrical resistivity and induced polarization imaging. *J. Appl. Geophys.* **2014**, *111*, 364–376.
56. Dahlin, T.; Leroux, V.; Nissen, J. Measuring techniques in induced polarisation imaging. *J. Appl. Geophys.* **2002**, *50*, 279–298.
57. Loke, M.; Barker, R. Rapid least-squares inversion of apparent resistivity pseudosections by a quasi-Newton method. *Geophys. Prospect.* **1996**, *44*, 131–152.
58. Loke, M.; Chambers, J.; Ogilvy, R. Inversion of 2D spectral induced polarization imaging data. *Geophys. Prospect.* **2006**, *54*, 287–301.
59. Caterina, D.; Beaujean, J.; Robert, T.; Nguyen, F. A comparison study of different image appraisal tools for electrical resistivity tomogrphy. *Surf. Geophys.* **2013**, *11*, 639–657.

60. MacNeill, J. *Electrical Conductivity of Soils and Rocks*; Geonics Limited: Mississauga, ON, Canada, 1980.
61. Portal, A.; Belle, P.; Mathieu, F.; Lachassagne, P.; Brisset, N. Identification and Characterization of Hard Rocks Weathering Profile by Electrical Resistivity Imaging. In Proceedings of the 23rd European Meeting of Environmental and Engineering Geophysics. European Association of Geoscientists & Engineers, Malmo, Sweden, 3–7 September 2017; Volume 2017, pp. 1–5.
62. Lamberty, P.; Geukens, F.; Marion, J. Notice explicative de la carte géologique Stavelot-Malmédy (50 5-6). Available online: https://orbi.uliege.be/handle/2268/207547 (accessed on 10 May 2020).
63. Modelska, M.; Buczyński, S.; Błachowicz, M.; Heidemann, M.; Grzęda, O.; Karkoszka, Ł. The Mofetta Tylicz–an example of carbonated water springs in the area of Tylicz (Beskid Sądecki, the Carpathians). *Geosci. Rec.* **2015**, *1*, 27–33.
64. Operacz, A.; Wąsik, E.; Hajduga, M.; Chmielowski, K. Therapeutic water in the Poprad Valley–the newest development in the polish outer Carpathians. *Pol. J. Environ. Stud.* **2018**, *27*, 1207–1217.
65. Jeong, C.H.; Kim, H.J.; Lee, S.Y. Hydrochemistry and genesis of CO2-rich springs from Mesozoic granitoids and their adjacent rocks in South Korea. *Geochem. J.* **2005**, *39*, 517–530.
66. Chae, G.; Yu, S.; Jo, M.; Choi, B.Y.; Kim, T.; Koh, D.C.; Yun, Y.Y.; Yun, S.T.; Kim, J.C. Monitoring of CO_2-rich waters with low pH and low EC: An analogue study of CO_2 leakage intro into shallow aquifers. *Environ. Eath Sci.* **2016**, *75*, 15.
67. Langmuir, D. *Aqueous Environmental Geochemistry*; Prentice Hall: Upper Saddle River, NJ, USA, 1997.
68. Aal, G.A.; Atekwana, E.; Revil, A. Geophysical signatures of disseminated iron minerals: A proxy for understanding subsurface biophysicochemical processes. *J. Geophys. Res. Biogeosci.* **2014**, *119*, 1831–1849.
69. Slater, L.; Choi, J.; Wu, Y. Electrical properties of iron-sand columns: Implications for induced polarization investigation and performance monitoring of iron-wall barriers. *Geophysics* **2005**, *70*, G87–G94.
70. Evrard, M.; Dumont, G.; Hermans, T.; Chouteau, M.; Francis, O.; Pirard, E.; Nguyen, F. Geophysical Investigation of the Pb–Zn Deposit of Lontzen–Poppelsberg, Belgium. *Minerals* **2018**, *8*, 233.
71. Moreira, C.; Borssatto, K.; Ilha, L.; Santos, S.; Rosa, F. Geophysical modeling in gold deposit through DC Resistivity and Induced Polarization methods. *REM-Int. Eng. J.* **2016**, *69*, 293–299.
72. Okay, G.; Cosenza, P.; Ghorbani, A.; Camerlynck, C.; Cabrera, J.; Florsch, N.; Revil, A. Localization and characterization of cracks in clay-rocks using frequency and time-domain induced polarization. *Geophys. Prospect.* **2013**, *61*, 134–152.
73. Krahenbuhl, R.; Hitzman, M. Geophysical modeling of two willemite deposits, Vazante (Brazil) and Beltana (Australia). In *SEG Technical Program Expanded Abstracts 2004*; Society of Exploration Geophysicists: Houston, TX, USA, 2004; pp. 1187–1190.
74. Dakir, I.; Benamara, A.; Aassoumi, H.; Ouallali, A.; Bahammou, Y.A. Application of Induced Polarization and Resistivity to the Determination of the Location of Metalliferous Veins in the Taroucht and Tabesbaste Areas (Eastern Anti-Atlas, Morocco). *Int. J. Geophys.* **2019**, *2019*, 1–11.
75. Pardo, O.; Gretta, C.; Alexander, E.; Iraida, M.; Pintor, B. Geophysical exploration of disseminated and stockwork deposits associated with plutonic intrusive rock: A case study on the eastern flank of Colombia's western cordillera. *Earth Sci. Res. J.* **2012**, *16*, 11–23.
76. Sultan, S.; Mansour, S.; Santos, F.; Helaly, A. Geophysical exploration for gold and associated minerals, case study: Wadi El Beida area, South Eastern Desert, Egypt. *J. Geophys. Eng.* **2009**, *6*, 345–356.
77. Azis, A.; Zamhuri, M.; Rais, M.; Aswad, S.; Patiung, O.; Sudianto, Y. Identify the Distribution of Galena using Induced Polarization and Resistivity Methods in central of Lombok, West Nusa Tenggara. In Proceedings of the IOP Conference Series: Earth and Environmental Science, Makassar, Indonesia, 1–2 November 2018; IOP Publishing: Bristol, UK, 2019; Volume 279.
78. Amaya, A.G.; Dahlin, T.; Barmen, G.; Rosberg, J.E. Electrical resistivity tomography and induced polarization for mapping the subsurface of alluvial fans: A case study in Punata (Bolivia). *Geosciences* **2016**, *6*, 51.
79. Yusof, M.A.A.; Ismail, N.; Muztaza, N. The Application of 2D Resistivity and Induced Polarization Methods for Slope Study at Penang Island, Malaysia. In Proceedings of the SEGJ 136th (Spring) Conference, Tokyo, Japan, 5–7 June 2017; The Society of Exploration Geophysicists of Japan: Tokyo, Japan, 2017.
80. Dahlin, T. *Application of Resistivity-IP to Mapping of Groundwater Contamination and Buried Waste*; Geophysical Association of Ireland: Dublin, Ireland, 2012; p. 6.
81. Leroux, V.; Dahlin, T.; Svensson, M. Dense resistivity and induced polarization profiling for a landfill restoration project at Härlöv, Southern Sweden. *Waste Manag. Res.* **2007**, *25*, 49–60.

82. Dahlin, T.; Rosqvist, H.; Leroux, V. Resistivity-IP mapping for landfill applications. *First Break* **2010**, *28*, 101–105.
83. Johansson, B.; Jones, S.; Dahlin, T.; Flyhammar, P. Comparisons of 2D-and 3D-inverted resistivity data as well as of resistivity-and IP-surveys on a landfill. In Proceedings of the Near Surface 2007-13th EAGE European Meeting of Environmental and Engineering Geophysics, Istanbul, Turkey, 3–5 September 2007.
84. Santos, F.A.M.; Almeida, E.P.; Castro, R.; Nolasco, R.; Mendes-Victor, L. A hydrogeological investigation using EM34 and SP surveys. *Earth Planets Space* **2002**, *54*, 655–662.
85. Marques, J.; Santos, M.F.; Graça, R.; Castro, R.; Aires-Barros, L.; Victor, L.M. A geochemical and geophysical approach to derive a conceptual circulation model of CO 2-rich mineral waters: A case study of Vilarelho da Raia, northern Portugal. *Hydrogeol. J.* **2001**, *9*, 584–596.